

Impurity accumulation in the main plasma and radiation processes in the divertor plasma of JT-60U

T. Nakano, H. Kubo, N. Asakura, K. Shimizu and S. Higashijima

Japan Atomic Energy Agency, Naka, Ibaraki-ken, 311-0193 Japan

e-mail contact of main author: nakano.tomohide@jaea.go.jp

Abstract. Two studies are included: tungsten accumulation in the main plasma and radiation processes of carbon ions in the detached plasma of JT-60U. [Tungsten] It has been found that tungsten accumulation becomes more significant with increasing plasma rotation velocity against the plasma current direction, where negative radial electric field is formed. The accumulation level does not depend on the tungsten generation flux, suggesting the transport plays a dominant role to determine the accumulation level. In a high density plasma at 62% of the Greenwald density, the tungsten accumulation levels decreased significantly, suggesting a shielding effect of the peripheral plasma. [Carbon] The spectral lines of C^{2+} and C^{3+} emitted around the X-point in the detached plasma with MARFE are measured with a VUV spectrometer and a 2-dimensional visible spectrometer in order to compare the generation flux of C^{3+} (ionization of C^{2+} and recombination of C^{4+}) and the loss flux of C^{3+} (ionization and recombination of C^{3+}). It has been found that C^{3+} is produced by the volume recombination of C^{4+} and the ionization of C^{2+} comparably. In contrast, the volume recombination of C^{3+} is not detected, and the ionization flux of C^{3+} is less than 1% of the C^{3+} generation flux. Thus, the C^{3+} generation flux is higher by two orders of magnitude than the loss flux. This result suggests that another loss mechanism of C^{3+} such as transport loss from the X-point is significant.

1 Impurity accumulation in the main plasma of JT-60U

1.1 Introduction

Tungsten (W) is one of the most promising materials for plasma facing components in future fusion devices such as ITER because of low sputtering yield, low hydrogen retention and high melting point. However, because of significant radiation loss from highly charged W ions, the allowable W concentration in the core plasma is estimated to be lower than 1×10^{-5} against the electron density. Compatibility of tungsten as a plasma facing material has been investigated with the first wall fully W-coated in AUG [1]. However, the results of the experiments are not sufficient to predict the impacts of the W wall in the future devices, because of low heat and particle flux to the

W plates, resulting in low W generation. In addition, because of low temperature in the core plasma, W ion charge state is much lower than those expected in ITER. Hence experiments in

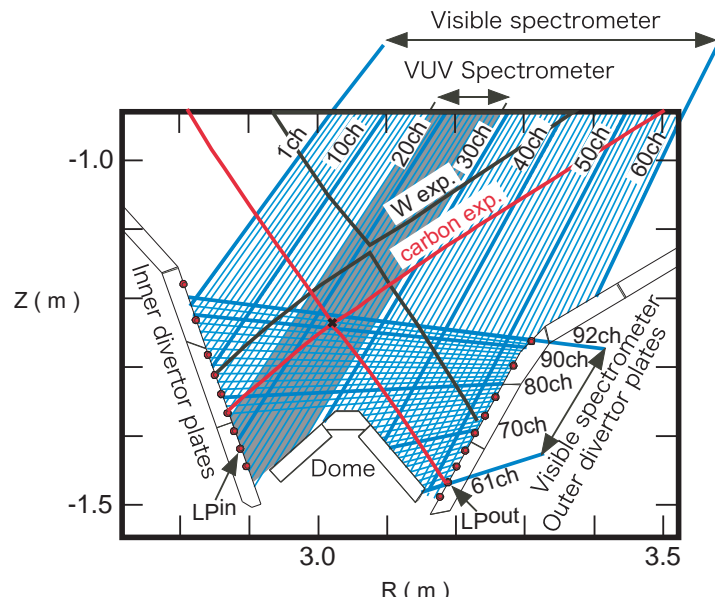


FIG. 1: The W-shaped divertor structure, the separatrix, the viewing chords (60 vertical and 32 horizontal) for the 2-dimensional visible spectrometer, the viewing chord for the vacuum-ultra-violet spectrometer, and the positions of the Langmuir probes, which are indicated by LP. The tungsten-coated tile is indicated by the shade.

large devices with high temperature and high plasma stored energy, associating high heat and particle flux to the W target plates by ELMs, are required to provide better predictions for the compatibility of the W wall. In JT-60U, W transport from the W-coated outer divertor tiles (12 tiles, covering 1/21 toroidal length) has been investigated with I_p of 1.5 MA, B_T of 3.3 T, $T_e(0)$ of > 5 keV, $n_e(0)$ of $6 \times 10^{19} \text{ m}^{-3}$ and the plasma stored energy of 3 MJ.

1.2 Experimental

JT-60U [2] is a tokamak with a major radius of 3.5 m and a minor radius of 1.0 m. Figure 1 shows a schematic view of the poloidal cross-section of the JT-60U divertor. Carbon fiber composite (CFC) materials are used for the divertor plates and the dome plates except for the inner dome wing plate, which is made of isotropic graphite. Tungsten-coated tiles at a thickness of 50 μm are used as upper divertor tiles. The number of tungsten-coated tiles is 12 ($\sim 1/21$ of the toroidal length). The tungsten generation flux is determined from the W I intensity (400.9 nm), measured by a visible spectrometer along the viewing chord number 51 of the visible vertical array. The core accumulation level of tungsten is determined from the W XLV (~ 6 nm) intensity measured by a VUV spectrometer for the main plasma [3].

Figure 2 shows waveforms of an H-mode discharge with the outer strike point on the W-coated tile at a plasma current of 1.5 MA and a toroidal magnetic field of 3.3 T. Until $t = 7.0$ s, the Co. tangential neutral beams (in the same direction of the plasma current) were injected by the same number of injectors as the CTR. tangential neutral beams (in the opposite direction), resulting in nearly zero toroidal plasma rotation as shown in Fig. 2 (b). Then at $t = 7.0$ s, the Co. beams are replaced with the Perp. beams, leading to negative plasma rotation (in the opposite direction to the plasma current). After $t = 7.0$ s, the W XLV intensity gradually increases while the W I intensity is nearly constant.

To investigate the W accumulation level, the rotation scan experiment were performed. In addition, to investigate the Z-dependence of the accumulation, similar rotation scan experiment were performed for Ar and Kr with the outer strike point not on the W-coated tiles.

1.3 Results and discussion

Figure 3 shows the dependence of W accumulation on the toroidal rotation velocity. Here, the W accumulation is defined as W XLV intensity divided by W I intensity and the electron density at the plasma center.

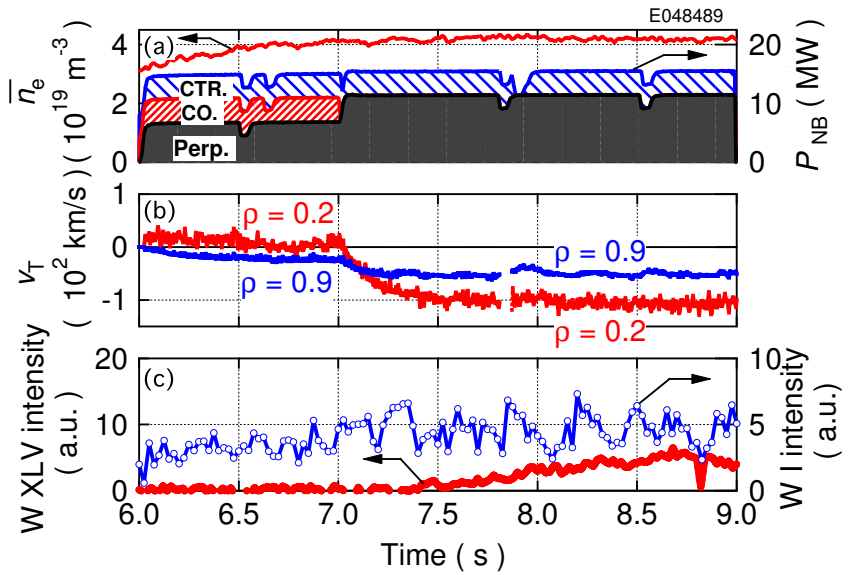


FIG. 2: Waveforms of (a) a line-averaged electron density, NB heating power (CTR, CO and Perp indicate, respectively, tangential beam lines in the same direction, that in the opposite direction and in the perpendicular direction to the plasma current, (b) plasma rotation velocity at a minor radius of 0.2 m and 0.9 m and (c) W XLV intensity from the main plasma and W I intensity from the divertor plasma.

Similar definition is used for Ar and Kr accumulation levels. In the positive rotation range ($v_T > 0$), the W XLV intensity is weak while the W I intensity is at a certain level, leading to low W accumulation. Around the rotation velocity of -0.5×10^5 m/s, with decreasing rotation velocity, the W XLV intensity increases while the W I intensity is constant. This results in an increase of the W accumulation with decreasing toroidal rotation velocity. Fur-

ther, with decreasing rotation velocity, the W XLV intensity increases while the W I intensity decrease. This results in significant W accumulation although the reason for the decrease of the W I intensity is not known.

In contrast to the W accumulation level, the Kr accumulation level is moderate although the Kr accumulation becomes significant with decreasing rotation velocity. Further the Ar accumulation is the lowest of the three species although the accumulation trend is similar to Kr and W. Comparison of the W accumulation level to the Kr and the Ar accumulation level suggests Z-dependence of the accumulation. The plasma transport code, named TOPICS, indicates that the negative toroidal plasma rotation results in negative radial electric field and that the strength of the electric field becomes high with decreasing rotation velocity. Thus, the radial electric field presumably plays a role for the Z-dependence of the accumulation.

In the discharge with a line-averaged electron density of 62% of the Greenwald density, where the outer divertor plasma is close to detachment, the W XLV intensity is very weak while the W I intensity is still detectable, leading to low W accumulation level. This result indicates that high density peripheral plasma is effective in shielding the W penetration into the main plasma.

1.4 Summary

With decreasing plasma toroidal rotation velocity, the Ar, the Kr and the W accumulation level become significant. However, the accumulation level tends to be significant in the order of Z number, *i.e.*, Ar, Kr and W, indicating Z-dependence of the accumulation. According to the calculation results of the plasma transport code, the negative radial electric field becomes strong with decreasing plasma toroidal rotation velocity. Thus, the radial electric field presumably plays a role for the Z-dependence of the accumulation. Further, it is shown that W penetration is suppressed in the high density plasma.

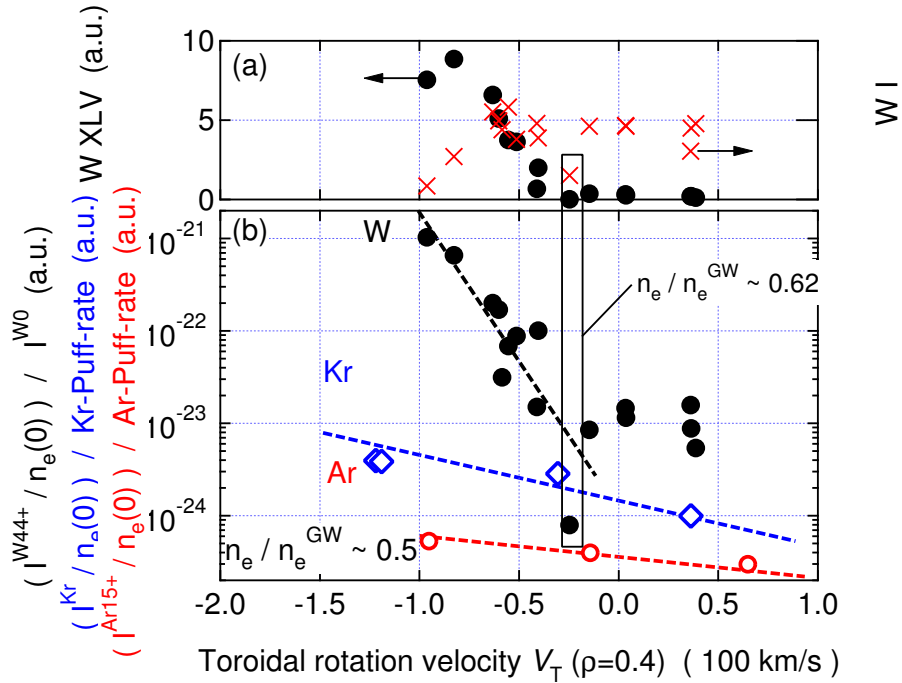


FIG. 3: (a) W XLV and W I intensity and (b) W, Kr and Ar accumulation level as a function of toroidal rotation velocity at a minor radius of 0.4 m. Dashed lines are to guide reader's eye.

2 Radiation process of carbon ions in the divertor plasma of JT-60U

Heat and particle control in a fusion reactor depends on whether the plasma flowing into the divertor is cooled sufficiently and whether the cold plasma such as a detached plasma is maintained. Remote radiative cooling, which is effective in detached plasmas, is one of the most straightforward methods. In tokamak devices with carbon tiles such as JT-60U [4] and DIII-D [5], it has been found that C^{3+} is one of the most dominant radiators in divertor plasmas, which contributes more than 60% of the total radiation power although C^{2+} is the strongest radiator in JET [6]. However, the source of the radiators has not been known: from which region, the main plasma or the divertor target plates, they flow into the radiative zone. In addition, the contribution fraction of C^{2+} and C^{3+} to the total radiation power is also unknown. Recently, it is reported that at the X-point in the detached plasma with MARFE, the volume recombination of C^{4+} was one of the processes to produce C^{3+} and that the electron temperature was too low for C^{3+} to ionize to C^{4+} [7]. More recently, it is reported that the ionization of C^{2+} was also one of the sources for C^{3+} and that the volume recombination of C^{3+} was not detected [8]. The present paper briefly summarizes the balance of ionization and recombination fluxes between C^{2+} , C^{3+} and C^{4+} , and the radiation power fraction of C^{2+} and C^{3+} to the total radiation power based on these two works [7, 8].

2.1 Experimental

Figure 1 shows the viewing chords for the visible spectroscopic measurement. The divertor region is covered with a spatial resolution of ~ 1 cm by 60 vertical and 32 horizontal viewing chords. Emission from the divertor plasma is transmitted to a visible spectrometer through optical fibers with a core diameter of 200 μm . A grating with 300 grooves / mm is used to cover a wide spectral range of 350 - 800 nm. The entrance slit width was set at 30 μm , leading to an instrumental width of 0.74 nm on the wavelength scale, and the frame rate of the CCD camera was set at 275 ms (an exposure time of 50 ms plus a digitization time of 225 ms). The detailed specification and setup of the spectrometer are found in Ref. [7]. With this spectrometer, the spectral lines of C III ($4f^3F - 5g^3G$: 407.0 nm), C III ($3s^3S - 3p^3P$: 464.7 nm), C III ($3p^1P - 3d^1D$: 569.6 nm), C III ($5d^3D - 6f^3F$: 748.7 nm), C IV ($3s^2S_{1/2} - 3p^2P_{3/2}$: 580.1 nm), C IV ($n = 5p - 6d$: 444.1 nm), C IV ($n = 6 - 7$: 772.6 nm), C IV ($n = 7 - 9$: 706.2 nm) and C IV ($n = 7 - 10$: 547.1 nm) were measured simultaneously with the 92 viewing chords. In Fig. 1, the viewing chord for a VUV (Vacuum Ultra Violet) spectrometer [3] is shown, which corresponds to 17 - 29 ch of the viewing chords of the visible spectrometer. The spectral range of 20 - 120 nm is covered and the dispersion at a wavelength of 35 nm is 2.4 nm / mm. The absolute sensitivity of the spectrometer was calibrated by a branching ratio method. The determined sensitivity was nearly constant in the wavelength range of 30-70 nm, and this is consistent with the sensitivity relatively calibrated with a synchrotron radiation light source [9]. The detailed specification and setup of the spectrometer is found in Refs. [3] and [7], respectively. With this spectrometer, the spectral lines of C III ($2p^3P - 3d^3D$: 45.96 nm), C III ($2p^3P - 3s^3S$: 53.83 nm), C III ($2p^1P - 3d^1D$: 57.43 nm), C III ($2s^1S - 2p^1P$: 97.70 nm) C IV ($2p^2P - 3s^2S$: 41.97 nm), C IV ($2s^2S - 3p^2P$: 31.24 nm), C IV ($2p^2D - 3d^2D$: 38.42 nm), C IV ($2p^2P - 4s^2S$: 29.70 nm), C IV ($2s^2S - 4p^2P$: 24.49 nm) and C IV ($2p^2D - 4d^2D$: 28.92 nm) were measured simultaneously.

Figure 1 also shows the positions of Langmuir probes and the viewing chords of a bolometer, which are similar to the vertical viewing chords for the visible spectrometer although the spatial resolution is ~ 4 cm. Hereafter, the viewing chords of the bolometer are labeled by the viewing chord numbers corresponding to the vertical array for the visible spectrometer.

The present spectroscopic measurement was performed for an L-mode plasma at a plasma cur-

rent of 1.0 MA and a toroidal magnetic field of 3.5 T with an X-point MARFE. In order to reduce statistical errors, the time-averaged intensities of the C III and C IV lines for 1.65 s (6 frames) during the MARFE phase are analyzed.

2.2 Analysis model

The population densities of the excited levels of C^{2+} are analyzed with a collisional-radiative model. The collisional-radiative model also calculates a line-radiation energy rate per C III photon and ionization/recombination events per C III photon. By using these coefficients, the line-radiation power from C^{2+} and the recombination and the ionization flux are evaluated from the C III brightness. Similar analyses are performed for C^{3+} with a collisional-radiative model for C^{3+} .

The temporal development of the population density of C^{i+} , $n_{C^{i+}(p)}$, where $i = 2, 3$, is expressed as the differential equation,

$$\begin{aligned} \frac{d}{dt} n_{C^{i+}(p)} &= - \left\{ \sum_{q < p} A(p, q) + \sum_{q \neq p} C(p, q) n_e + S(p) n_e \right\} n_{C^{i+}(p)} \\ &\quad + \sum_{q > p} A(q, p) n_{C^{i+}(q)} + \sum_{q \neq p} C(q, p) n_e n_{C^{i+}(q)} \\ &\quad + \left\{ \alpha(p) n_e + \beta(p) + \gamma(p) \right\} n_{C^{(i+1)+}} n_e \\ &\quad + \sum_n q^{CX}(n, p) n_{D^0(n)} n_{C^{(i+1)+}}, \end{aligned} \quad (1)$$

which is coupled with similar equations for other levels. Here p and q stand for a level that is determined by a principal quantum number n or combination of n and an azimuthal quantum number l . In Eq.(1), $q < p$ means that level q lies energetically lower than level p . The spontaneous transition probability from level p to level q is denoted by $A(p, q)$. The rate coefficients for electron impact excitation if $p < q$ (de-excitation if $p > q$) and ionization are denoted by $C(p, q)$ and $S(p)$, respectively. The rate coefficients for three-body, radiative and di-electronic recombination are denoted by $\alpha(p)$, $\beta(p)$, and $\gamma(p)$, respectively. These rate coefficients are functions of electron temperature T_e . The rate coefficient for the charge exchange recombination from $D^0(n)$ to C^{i+} is denoted by $q^{CX}(n, p)$, which is a function of impact energy between $D^0(n)$ and C^{i+} . In Eq.(1), n_e , $n_{C^{i+}}$ and $n_{D^0(n)}$ denote electron density, C^{3+} density and $D^0(n)$ population density, respectively. On the assumption that the quasi-steady-state solution is valid, the time derivative of Eq.(1) can be set at 0. Then the set of coupled differential equations reduces to the set of coupled linear equations. The steady-state solution for the population density of C^{i+} is obtained as

$$n_{C^{i+}(p)} = R_0(p) n_e n_{C^{i+}} + R_1(p) n_e n_{C^{(i+1)+}} + R_{CX}(p) n_{D^0} n_{C^{(i+1)+}}, \quad (2)$$

where $n_{C^{i+}}$ denotes the ground-state density of C^{i+} . Here, $R_0(p)$ and $R_1(p)$ are population coefficients as functions of T_e and n_e , while $R_{CX}(p)$ is a population coefficient as functions of T_e , n_e , and the impact energy between D^0 and $C^{(i+1)+}$. The first term of Eq.(2) is referred to as the ionizing plasma component, $n_{C^{i+}(p)}^{ioniz.}$, the second term as the recombining plasma component, $n_{C^{i+}(p)}^{recomb.}$, and the third term as the charge exchange (CX) recombining plasma component, $n_{C^{i+}(p)}^{CX}$. The calculated population density of C^{2+} for the ionizing plasma component and those of C^{3+} for the ionizing and the recombining plasma component are shown in Figs. 4 (a) and (b), respectively, as a function of the term energy of the upper level of the transition, or the energy

from the ground state. In comparison with the measured population density, the population density is divided by the statistical weight, $w_g(p)$. Here, $w_g(p) = 2p^2$ if p is the principal quantum number.

2.3 Results

2.3.1 Population analysis

The line-integrated population density is inferred from the following equation, $n_{C^{i+}(p)}^{meas.} L = I(p, q) / A(p, q) (\text{m}^{-2})$. Here $I(p, q)$ ($\text{ph m}^{-2}\text{s}^{-1}$) is the measured C III or C IV brightness, and L (m) the length of the emission zone along a viewing chord. Further, the population density is divided by the statistical weight of the upper level of the transition, $w_g(p)$. In Figs. 4 (a) and (b), respectively, the population densities from the VUV C III and C IV lines are plotted together with those from the visible C III and C IV lines, which are volume-averaged for the same observation volume as the VUV spectrometer, which corresponds to the volume between 17 ch and 29 ch. To fit the measured C III population densities with those calculated by the collisional-radiative model, a regression analysis was performed with the electron temperature, the electron density, the neutral deuterium density and the ratio of C^{3+} to C^{2+} density as the free parameters, on the assumption that temperatures of a neutral deuterium and a C^{3+} ion were equal to the electron temperature. As shown in the figure, the result of the regression analysis indicates that the ionizing plasma component dominates the population density, meaning that the recombining plasma component is not detected. The determined electron temperature and density are 7.8 eV and $1.0 \times 10^{20} \text{ m}^{-3}$, respectively. Note that the charge exchange recombining plasma component is absent because the residual between the regression curve and the measured population densities becomes large with increasing neutral deuterium density over zero. The mean-free-path of a neutral deuterium, calculated from an ionization rate coefficient ($7.3 \times 10^{-15} \text{ m}^3\text{s}^{-1}$) at an electron temperature of 7.8 eV and density of $1.0 \times 10^{20} \text{ m}^{-3}$, taken from Ref. [10], is 3.5 cm on the assumption that the neutral deuterium temperature is equal to the electron temperature. Given that the spatial spread of the strong C III emission zone is $\sim 20 \text{ cm}$, where the viewing chord interval is $\sim 1 \text{ cm}$, it is considered that the

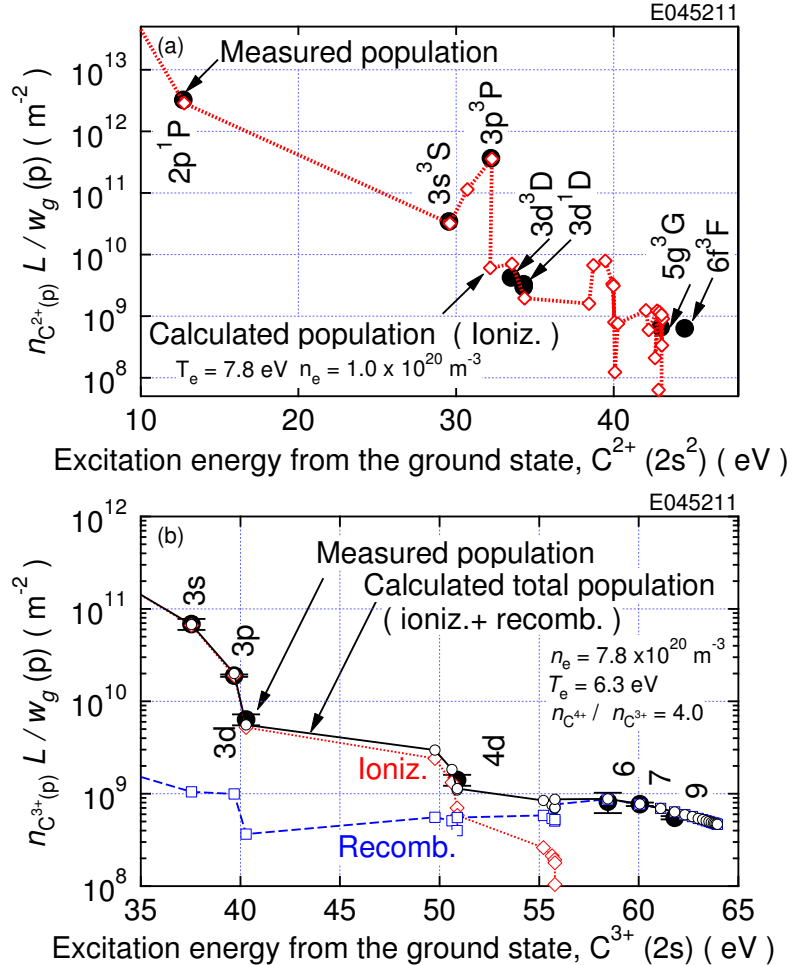


FIG. 4: Comparison of measured line-integrated population density and fitted population density, divided by the statistical weight, as a function of term energy of the excited level (a) for C III and (b) C IV.

deuterium and a C^{3+} ion were equal to the electron temperature. As shown in the figure, the result of the regression analysis indicates that the ionizing plasma component dominates the population density, meaning that the recombining plasma component is not detected. The determined electron temperature and density are 7.8 eV and $1.0 \times 10^{20} \text{ m}^{-3}$, respectively. Note that the charge exchange recombining plasma component is absent because the residual between the regression curve and the measured population densities becomes large with increasing neutral deuterium density over zero. The mean-free-path of a neutral deuterium, calculated from an ionization rate coefficient ($7.3 \times 10^{-15} \text{ m}^3\text{s}^{-1}$) at an electron temperature of 7.8 eV and density of $1.0 \times 10^{20} \text{ m}^{-3}$, taken from Ref. [10], is 3.5 cm on the assumption that the neutral deuterium temperature is equal to the electron temperature. Given that the spatial spread of the strong C III emission zone is $\sim 20 \text{ cm}$, where the viewing chord interval is $\sim 1 \text{ cm}$, it is considered that the

neutral deuterium penetration into this zone is limited. This estimation supports the collisional-radiative model analysis, which resulted in absence of the charge exchange recombining plasma component.

Similar analysis for C IV, shown in Fig. 4 (b) indicated that the recombining plasma component dominated the population density with levels ≥ 5 of C IV, which term energies are higher than 55 eV. This supports that the population densities of all the levels of C III is dominated by the ionizing plasma component because the ionization potential of C III (47.9 eV) is lower than the term energy of the $n = 5$ level of C IV (~ 56 eV).

2.3.2 Radiation power and ionization/recombination flux

The radiation power from the ionizing plasma component is evaluated from the absolute intensity of C III ($3s^3S - 3p^3P$) with the coefficient shown in Fig. 3 of Ref [8]. Given that the absolute intensity of C III ($3s^3S - 3p^3P$) averaged between the viewing chords 17 ch and 29 ch, which correspond to the viewing chord of the VUV spectrometer, is $4.0 \times 10^{20} \text{ ph m}^{-2}\text{s}^{-1}$ and that the 'radiation / C III ($3s^3S - 3p^3P$)' coefficient at an electron temperature of 7.8 eV and an electron density of $1.0 \times 10^{20} \text{ m}^{-3}$ is $1 \times 10^{-15} \text{ J ph}^{-1}$, then the radiation power of the ionizing plasma component is estimated to be 0.4 MW m^{-2} , which corresponds to 30 % of the total radiation power measured by the bolometer, 1.4 MW m^{-2} . Similar evaluation for C IV ionizing and recombining plasma component results in a radiation power of 0.8 MW m^{-2} (60% of the total radiation power) and 30 kW m^{-2} (2%), respectively.

The ionization flux of C^{2+} is evaluated in a similar way to the radiation power evaluation. As shown in Fig. 3 of [8], the 'ionization / C III ($3s^3S - 3p^3P$)' coefficient is 0.4 at an electron temperature of 7.8 eV and an electron density of $1.0 \times 10^{20} \text{ m}^{-3}$ and the absolute intensity of the C III line is $4.0 \times 10^{20} \text{ ph m}^{-2}\text{s}^{-1}$, leading to the C^{2+} ionization flux of $1.6 \times 10^{20} \text{ m}^{-2}\text{s}^{-1}$. Similar analysis for C IV results in an ionization flux of C^{3+} to C^{4+} of $2.0 \times 10^{18} \text{ m}^{-2}\text{s}^{-1}$ and a recombination flux of C^{4+} to C^{3+} of $2.2 \times 10^{20} \text{ m}^{-2}\text{s}^{-1}$.

2.4 Discussion and summary

The above evaluation are summarized in Fig. 5. The line-radiation power from the ionizing plasma component of C^{2+} and C^{3+} were evaluated to be, respectively 30% and 60% of the total radiation power while the line-radiation power from the recombining plasma component of C^{3+} was only a few percent. The C^{3+}

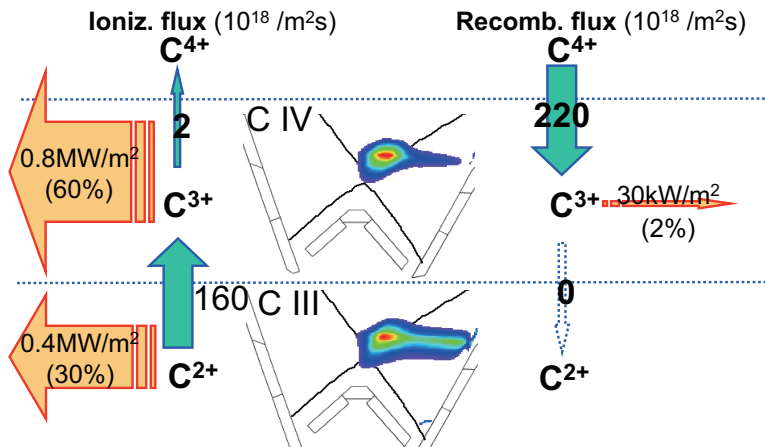


FIG. 5: From the left, the radiation from ionizing component, the ionization flux, the spatial distribution of the emissivity, the recombination flux, and the radiation from recombining component of C^{3+} (upper) and C^{2+} (lower).

production flux, *i.e.*, the recombination flux of C^{4+} into C^{3+} and the ionization flux of C^{2+} into C^{3+} were, respectively, 220 and $160 \times 10^{18} \text{ m}^{-2}\text{s}^{-1}$. In contrast, the C^{3+} loss flux, *i.e.*, the recombination flux of C^{3+} into C^{2+} was not detected and the ionization flux of C^{3+} into C^{4+} was $2 \times 10^{18} \text{ m}^{-2}\text{s}^{-1}$. Hence the C^{3+} production flux is higher by two orders of magnitude than

C^{3+} loss flux, suggesting that the C^{3+} ions around the X-point is lost by other processes than atomic processes such as transport related loss channels. The transport loss mechanism will be investigated with an improved impurity transport code such as IMPMC [11].

It is concluded that the dominant radiator, C^{3+} , is produced by ionization of C^{2+} and recombination of C^{4+} at similar rates around the X-point in the detached plasma. Because the ionization flux of C^{3+} is much smaller than the recombination flux of C^{4+} around the X-point, the predominant source of C^{4+} , which recombines into C^{3+} , is presumably the main plasma. Since the flux of C^{4+} is determined by the transport in the main plasma, it is difficult to control the C^{4+} flux. In contrast, significant ionization of C^{2+} into C^{3+} and no recombination of C^{3+} into C^{2+} indicate that the source of C^{2+} , which ionized into C^{3+} , exists in the divertor region, which can be controlled more easily for instance by seeding CD_4 . Because the source rate of C^{3+} from the main plasma (the recombination of C^{4+}) and the divertor (the ionization of C^{2+}) was found to be similar as described above, the radiation loss control by impurity seeding from the divertor may be possible although the controllability may not be high.

This work was partly supported by JSPS, Grant-in-Aid for Young Scientist (B) (19760602) and Scientific Research for Priority Areas (19055005).

Reference

- [1] Neu R., Dux R. *et.al* , *Nucl. Fusion* , **45** (2005) 209.
- [2] Kishimoto H., Ishida T. *et.al* , *Nucl. Fusion* , **45** (2005) 986.
- [3] Kubo H., Sugie T.*et.al* , *Rev. Sci. Instr.* **59** (1988) 1515.
- [4] Kubo H., Sugie T. *et.al* , *Plasma Phys. Control. Fusion* , **37** (1995) 1133.
- [5] Fenstermacher M. E., Allen S. L. *et.al* , *Phys. Plasmas* , **4** (1997) 1761.
- [6] Maggi C. F., Elder J. D. *et.al* , *J. Nucl. Mater.* **241-243** (1997) 414.
- [7] Nakano T., Kubo H. *et.al* , *Nucl. Fusion* , **47** (2007) 1458.
- [8] Nakano T., Kubo H. *et.al* , *submitted to J. Nucl. Mater.* (2008).
- [9] Sugie T., Kubo H. *et.al* , *JAERI-M 93-057* Japan Atomic Energy Research Institute (1993) 347.
- [10] Goto M., Sawada K. *et.al* , *Phys. Plasmas* **9** (2002) 4316.
- [11] Shimizu K., Takizuka T. *et.al* , *submitted to J. Nucl. Mater.* (2008).